

## RESEARCH ARTICLE

# Best Feed Positions and Radiation Patterns of Typical Multibeam Dielectric Lens Antenna

M. MUHSIN<sup>1,2</sup>, (Member, IEEE), KAMILIA KAMARDIN<sup>1,3</sup>, (Senior Member, IEEE),  
YOSHIHIDE YAMADA<sup>1</sup>, (Senior Member, IEEE), YOSHIKI SUGIMOTO<sup>4</sup>, (Member, IEEE),  
AND KUNIO SAKAKIBARA<sup>4</sup>, (Senior Member, IEEE)

<sup>1</sup>Malaysia-Japan International Institute of Technology, Universiti Teknologi Malaysia, Kuala Lumpur 54100, Malaysia

<sup>2</sup>School of Electrical Engineering, Telkom University Surabaya, Surabaya Campus, Surabaya 60231, Indonesia

<sup>3</sup>Wireless Communication Centre, Universiti Teknologi Malaysia, Kuala Lumpur 54100, Malaysia

<sup>4</sup>Department of Electrical and Mechanical Engineering, Nagoya Institute of Technology, Nagoya, Aichi 464-8555, Japan

Corresponding author: Kamilia Kamardin (kamilia@utm.my)

This work was supported in part by Universiti Teknologi Malaysia (UTM) through UTM Fundamental Research under Grant 22H39; and in part by the National Institute of Information and Communications Technology (NICT), Japan, under Commissioned Research under Grant 00401.

**ABSTRACT** Multibeam base station antennas are introduced for 5G and 6G mobile communication systems. Considering higher frequency bands such as millimeter waves for 5G and terahertz for 6G, dielectric lens antennas become promising candidates due to their simple antenna configuration and excellent multibeam radiation characteristics. Therefore, it is important to identify the best multibeam antenna from the existing typical lens antennas. In this article, a shaped lens and some conventional lenses are considered. For the conventional types, the hyperbolic-planar, plano-convex, and spherical-convex are selected. As for the shaped lens, Abbe's sine condition lens is selected. This research begins by finding the best feed position of four types of lenses. A MATLAB program is developed to find the smallest distance point for all focal region rays. Based on this point, the feed position is selected and multibeam radiation patterns of four lenses are obtained. It is shown that the spherical-convex lens can achieve the highest gain and the smallest beam shape degradation. High gain characteristics are obtained until a 35° beam shift. As for sidelobe characteristics, Abbe's sine condition lens has the lowest sidelobe level. These properties are then clarified using amplitude and phase distribution on the aperture plane. Furthermore, focal region ray concentration changes by  $F/D$  and refractive index are discussed for practical applications.

**INDEX TERMS** Focal region, ray tracing, multibeam antenna, lens antenna, millimeter wave.


## I. INTRODUCTION

In recent mobile wireless communications, 5G mobile becomes a practical application condition, while 6G mobile is currently developing [1], [2], [3], [4], [5], [6]. As for the access method, the massive multiple-input multiple-output (MIMO) is introduced [7], [8], [9], [10], [11]. Then, multibeam radiation characteristics are required, especially at the base station side. Moreover, the 5G mobile introduces the usage of the millimeter wave frequency, whereas the 6G mobile will introduce the terahertz frequency. At higher frequencies, base station antenna sizes become 10 centime-

ters or less. For this antenna size, a multibeam dielectric lens antenna is promising because of its simple structure and excellent multibeam performance.

Multibeam dielectric antennas are constructed by multiple feed antennas and a lens as shown in Fig. 1. Feed antennas are arranged at the optimum position. Then, the lens is used for beam focusing. Finally, multiple focused narrow beams can be obtained. In this configuration, the feed position and the lens shape should be optimized to meet the excellent multibeam characteristics.

The most famous multibeam lens antenna was the Luneburg lens. The lens was conformed of many annular spherical dielectric layers and the used lens was not homogeneous [12], [13], [14], [15]. By these configurations, the same radiation

The associate editor coordinating the review of this manuscript and approving it for publication was Gerardo Di Martino .

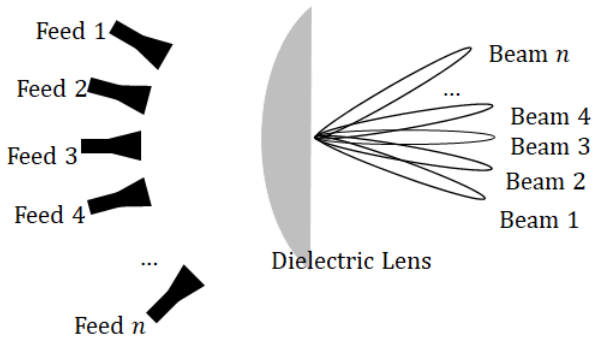


FIGURE 1. Multibeam dielectric lens antenna.

beam was obtained at any feed position on the sphere. However, the non-homogeneous structure was not easy to fabricate and unsuitable for practical application due to layered material.

Some variations of the non-homogeneous lenses have been proposed. A low-cost multibeam lens antenna for 5G communications is presented in [16]. This perforated planar lens structure achieved  $28^\circ$  beam scanning with a gain of over 18 dBi at 26 GHz. This beam scanning ability is considered insufficient for a wide-angle multibeam. A graded dielectric lens antenna is proposed in [17]. Layered materials with various dielectric constants are used. The lens is designed to cover a full  $360^\circ$  scanning angle which is divided into 8 sectors with 5.9 dBi gain at 5.8 GHz. The gain value is very high for 5G in millimeter waves.

As for the homogenous lens, conventional lens antennas of hyperbolic-planar, plano-convex, and spherical convex are exist [18], [19], [20], [21]. The lens surface of these lenses is given by simple equations making them very practical. However, multibeam radiation characteristics are not clarified.

For the homogenous good multibeam lens antenna, a shaped lens of Abbe's sine condition lens was developed. The shape of Abbe's sine condition lens is defined by some equations of conditions. Therefore, the best feed positions and multibeam radiation patterns are made clear [22].

Some modifications to the lens shape have been conducted by some research. Straight-line condition lens is presented in [23]. The straight-line condition offers a thin structure as compared to other lens shapes. Multibeam performance is obtained using the feed positions of Abbe's sine condition lens. However, these feed positions may not be the optimum position. A bifocal lens is proposed in [24]. This lens design employed two focal points to achieve good multibeam performance. The bifocal lens is then improved using the multiobjective optimization by multiple focusing points in [25]. However, this design method may result in a complex lens shape that is difficult to fabricate.

Some research related to feed positioning is presented as follows. A wide-scan spherical lens with multibeam ability is presented in [26]. The ball-shaped lens has a specific focal point for wide-angle coverage. The feed position is

determined by an equation concerning lens geometry and refractive index. Another work in [27] proposed an integrated lens antenna employing two lenses. Focal region ray tracing is used to examine how the rays are concentrated. The feed position is determined by looking for the most concentrated point and approached by using the locus approach. The use of meta-material to make a thin lens is presented in [28]. Feed antennas are arranged as a linear array configuration. By this arrangement, beam degradation is considerably high. These research studies emphasize the importance of selecting optimum feed positions. However, there is still no method to determine the best feed position which can be applied for any lens shapes.

This article proposes a method for determining the best feed position, then examines the properties of three different types of conventional lenses and Abbe's sine condition lens. To achieve optimal multibeam radiation patterns, the best feed positions should be determined. At these positions, multiple feed antennas are placed as shown in Fig. 1. These multiple feeds work simultaneously to perform multibeam radiation patterns. To find these feed positions, the MATLAB program for determining the best feed positions is developed. Based on the best feed positions of the four lenses, the characteristics of the multibeam radiation patterns are obtained by using electromagnetic simulator (FEKO) calculations. For a detailed comparison of multibeam radiation characteristics, cross-sectional shapes of multibeam and near-field distribution are obtained. Finally, the best lens type for an excellent multibeam radiation pattern is selected.

The rest of this article is organized as follows. The lens shape of three conventional lenses and Abbe's sine condition lens are provided in Section II. Meanwhile, the focal region ray tracing and feed position determination programs are presented in Section III. Then, the configuration of electromagnetic simulation is presented in Section IV. The obtained multibeam radiation patterns are presented later in Section V. Then discussion in near field distribution, the influence of  $F/D$  change, and the influence of refractive index change are presented in Section VI. Finally, conclusions are presented in Section VII.

## II. LENS TYPES

In this section, four types of lens shapes are selected: hyperbolic-planar, plano-convex, spherical-convex, and Abbe's sine condition lens. Hyperbolic-planar, plano-convex, and spherical-convex lenses are conventional lenses, whereas Abbe's sine condition lens is a shaped lens. The shape of a conventional lens is based on a simple equation while the shaped lens is based on a shaping method.

### A. HYPERBOLIC-PLANAR LENS

Fig. 2 shows the geometry of the hyperbolic-planar lens. The inner surface is formed by a hyperbolic shape and the outer surface is a planar. The inner surface is given by  $r$  at  $\theta$

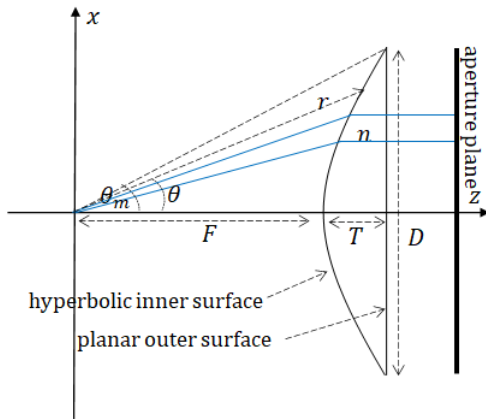


FIGURE 2. Geometry of hyperbolic-planar lens.

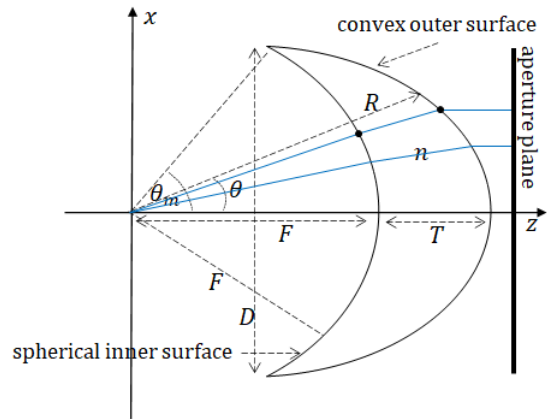


FIGURE 4. Geometry of spherical-convex lens.

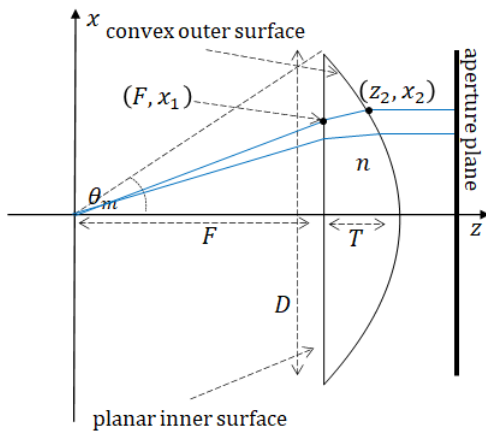


FIGURE 3. Geometry of plano-convex lens.

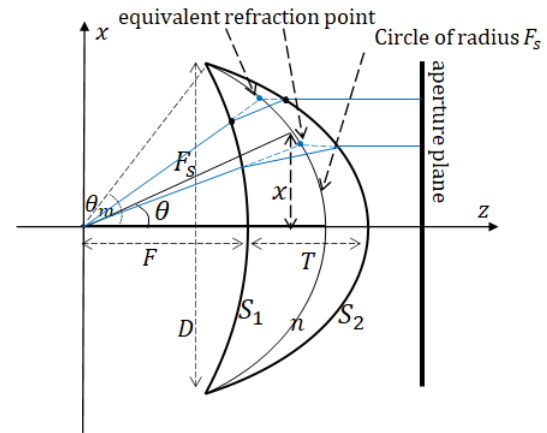


FIGURE 5. Geometry of Abbe's sine condition lens.

angle [19]

$$r = \frac{(n - 1) F}{n \cos \theta - 1}. \quad (1)$$

Here,  $F$  is the focal length,  $D$  is the diameter, and  $n$  is the refractive index of the lens.  $T$  shows the lens thickness.

**B. PLANO-CONVEX LENS**

Fig. 3 shows the geometry of the plano-convex lens. The inner surface is flat and the outer surface is convex. The flat inner surface is given by  $(F, x_1)$ . Then, the convex shape of the outer surface is given by  $(z_2, x_2)$  where [19]

$$z_2 = \frac{[(n - 1) T - M] \sqrt{(n^2 - 1) x_1^2 + n^2 F^2} + n^2 F M}{n^2 M - \sqrt{(n^2 - 1) x_1^2 + n^2 F^2}} \quad (2)$$

and

$$x_2 = x_1 \left[ 1 + \frac{z_2 - F}{\sqrt{(n^2 - 1) x_1^2 + n^2 F^2}} \right]. \quad (3)$$

Here  $M = \sqrt{F^2 + x_1^2}$ .

**C. SPHERICAL-CONVEX LENS**

Fig. 4 shows the geometry of a spherical-convex lens. The inner surface is spherical with a constant distance of  $F$  from the focal center. The outer surface is defined by [19]

$$R = \frac{(n - 1) (F + T)}{n - \cos \theta}. \quad (4)$$

Here,  $T$  is the lens thickness

$$T = \frac{2F - \sqrt{4F^2 - D^2}}{2(n - 1)}. \quad (5)$$

**D. ABBE'S SINE CONDITION LENS**

Abbe's sine condition lens is categorized as a shaped lens. The geometry of Abbe's sine condition lens is shown in Fig. 5. The shape of this lens is determined by two differential equations at inner surface  $S_1$ , the outer surface  $S_2$  [23], [29], and the lens shape differential equation is derived from the equivalent refraction point given by [19]

$$x = F_s \sin \theta, \quad (6)$$

$$\frac{dx}{d\theta} = F_s \cos \theta. \quad (7)$$

Here,  $F_s$  is the radius of a circle.

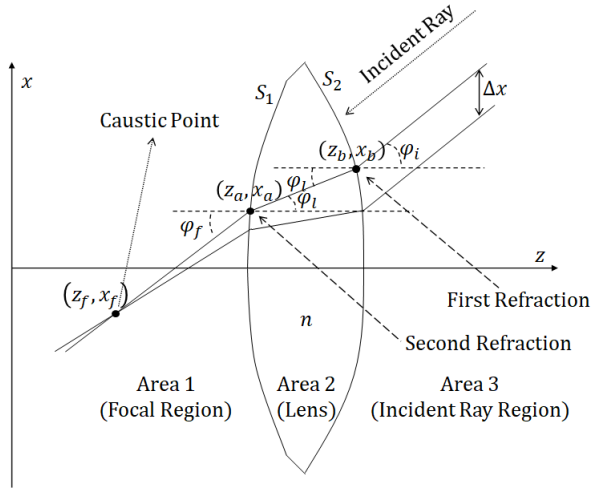


FIGURE 6. Receiving mode ray tracing concept.

TABLE 1. Parameters of four types lens antenna.

	n	F (mm)	D (mm)	$\theta_m$ (°)	T (mm)
Hyperbolic-Planar Lens	2	120	200	33.65	30.24
Plano-Convex Lens	2	120	200	39.81	36.22
Spherical-Convex Lens	2	120	200	56.44	53.67
Abbe's Sine Condition Lens	2	120	200	43.23	39.62

### III. FOCAL REGION RAY TRACING

To examine the multibeam radiation patterns of the four types of lens selected, a problem in determining the adequate feed positions arises. The most promising method is to calculate the focal region rays for parallel incident rays. The calculation method is called the receiving mode ray tracing as shown in Fig. 6. The incident ray direction is selected based on the target beam direction ( $\phi_i$ ). The incident ray arrives on the lens at point  $(z_b, x_b)$  and comes out at point  $(z_a, x_a)$ . In the focal region, the ray from the lens passes at an angle  $\phi_f$ . Many rays in the focal region may be concentrated at the caustic point. This caustic point can be considered the best feed point. In performing the receiving mode ray tracing, the parameters of the four types of lens parameters are summarised in Table 1.

#### A. RAY TRACING METHOD

The ray tracing process is divided into 3 steps as shown in Fig. 7. These 3 steps are explained as follows.

##### 1) FINDING REFRACTION POINT ON OUTER SURFACE (STEP 1)

Incident rays arrive on the outer surface  $S_2$  at  $P_2 = (z_b, x_b)$ . Surface  $S_2$  is determined from discrete points shown by the black points, i.e.,  $(z_q, x_q)$ . The incident ray is expressed by

$$z \tan \phi_i = x - x_i. \quad (8)$$

By changing  $x_i$ , many incident rays are obtained. Then, the MATLAB function of “polyxpoly” is used to find

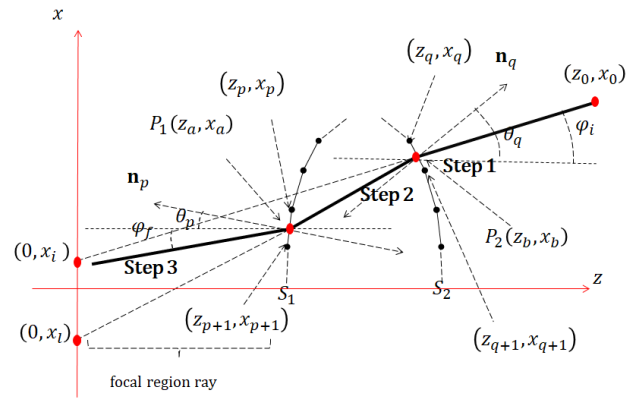


FIGURE 7. Steps of receiving mode ray tracing.

$P_2 = (z_b, x_b)$  as an intersection between the lens outer surface and the extended incident ray (8). At this intersection point, the first refraction is obtained. The angle  $\theta_q$  of the normal vector  $\mathbf{n}_q$  at this point can be calculated from the two nearest points of  $(z_q, x_q)$  and  $(z_{q+1}, x_{q+1})$  as

$$\sin \theta_q = \frac{z_{q+1} - z_q}{\sqrt{(x_{q+1} - x_q)^2 + (z_{q+1} - z_q)^2}}. \quad (9)$$

This normal vector angle is important to define the refracted rays from the outer surface.

##### 2) FINDING REFRACTION POINT ON INNER SURFACE (STEP 2)

By using the normal vector angle  $\theta_q$ , a ray inside the lens can be drawn. The refracted ray from the outer surface can be calculated by following Snell’s law of

$$n = \frac{\sin(\phi_i - \theta_q)}{\sin(\phi_l - \theta_q)}. \quad (10)$$

Here  $\phi_l$  is the refracted angle.

The ray inside the lens is then expressed as

$$z - z_b = \tan \phi_l (x - x_b). \quad (11)$$

The same procedure using the MATLAB function of “polyxpoly” between the lens inner surface  $S_1$  and the ray inside the lens (11) is conducted to find the refraction point  $P_1 = (z_a, x_a)$ . In this refraction point, angle  $\theta_p$  of the normal vector  $\mathbf{n}_p$  can be calculated from the two nearest points of  $(z_p, x_p)$  and  $(z_{p+1}, x_{p+1})$  as

$$\sin \theta_p = \frac{z_{p+1} - z_p}{\sqrt{(x_{p+1} - x_p)^2 + (z_{p+1} - z_p)^2}}. \quad (12)$$

The normal vector angle is then used to draw the focal region ray in the next step.

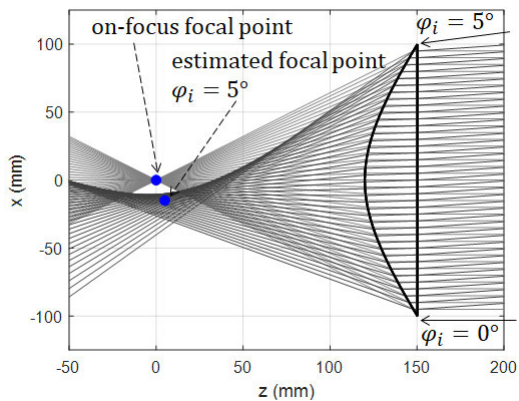


FIGURE 8. On-focus and 5° off-focus receiving mode ray tracing of hyperbolic-planar lens.

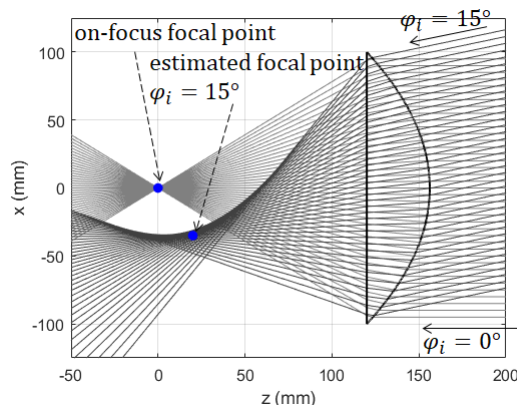


FIGURE 9. On-focus and 15° off-focus receiving mode ray tracing of plano-convex lens.

### 3) FOCAL REGION RAY (STEP 3)

The refracted ray on the inner surface follows Snell's law as

$$n = \frac{\sin(\varphi_f - \theta_p)}{\sin(\varphi_l - \theta_p)} \quad (13)$$

where  $\varphi_f$  is the refracted angle of the ray in the focal region. The final focal region ray is then drawn from  $P_1$  with an angle of  $\varphi_f$  as

$$z - z_a = \tan \varphi_f (x - x_a). \quad (14)$$

After the whole process is repeated for each parallel incident ray, many final refracted rays can be obtained. These rays can be analyzed to find the best feed position.

### B. RAY CONCENTRATION

The ray concentration performance of the four types of lenses is examined. Converged points with good ray concentration are expected. If the rays are concentrated, the feed position can be decided confidently. Otherwise, it becomes hard to decide the feed position. To make a good comparison, the key parameters such as refractive index, focal length, and diameter are equally set. Parameters of these four types of lenses are presented in Table 1.

Results of the hyperbolic-planar lens are shown in Fig. 8. The focal region rays are perfectly converged at incident angle  $\varphi_i = 0^\circ$ . Meanwhile, the diverged focal region rays are observed at  $\varphi_i = 5^\circ$ . The most concentrated point will be determined by finding the throat point. The estimated throat point is (5, -15). At larger incident angles ( $\varphi_i > 5^\circ$ ), focal rays diverge and become larger. Selection of feed position becomes more difficult.

Results of the plano-convex lens are shown in Fig. 9. Focal region rays are perfectly converged at incident angle  $\varphi_i = 0^\circ$ . Whereas, the diverged focal region rays are observed at  $\varphi_i = 15^\circ$ . Similar to the hyperbolic-planar lens, the most concentrated point will be determined by finding the throat point. The estimated throat point is (20, -35). At larger incident angles ( $\varphi_i > 15^\circ$ ), the focal rays diverge and become larger. Selection of feed position becomes more difficult.

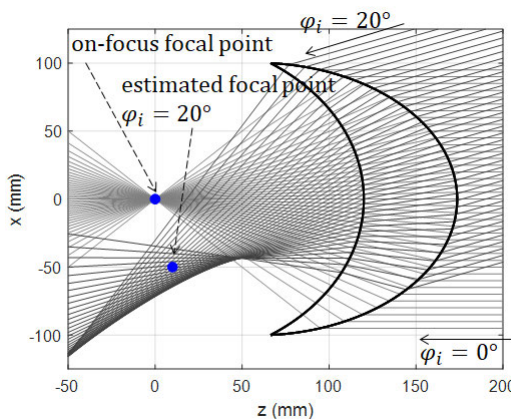


FIGURE 10. On-focus and 20° off-focus receiving mode ray tracing of spherical-convex lens.

Results of the spherical-convex lens are shown in Fig. 10. Focal region rays are perfectly converged at incident angle  $\varphi_i = 0^\circ$ . The diverged focal region rays are observed at  $\varphi_i = 20^\circ$ , while the estimated focal point of this incident angle is at (10, -50). At larger incident angles ( $\varphi_i > 20^\circ$ ), the focal region rays become more diverged. Selection of feed position at these larger incident angles is more difficult.

Results of the Abbe's sine condition lens are shown in Fig. 11. Focal region rays are perfectly converged at incident angle  $\varphi_i = 0^\circ$ . The diverged focal rays are observed at  $\varphi_i = 30^\circ$ , while the estimated focal point of this incident angle is at (65, -50). At larger incident angles  $\varphi_i > 30^\circ$ , the selection of feed position is more difficult.

The summary of the estimated focal points of Fig. 8 - 11 are shown in Fig. 12. Abbe's sine condition (Abbe) lens has the throat part up to an incident angle  $\varphi_i = 30^\circ$ . The hyperbolic-planar (Hy-Pla), plano-convex (Pla-Con), and spherical-convex (Sphe-Con) lens has a throat part at incident angles up to 5°, 15°, and 20°, respectively. Therefore, finding suitable feed positions for higher incident angles becomes a problem. Thus, a more robust mechanism to find suitable feed positions is required.

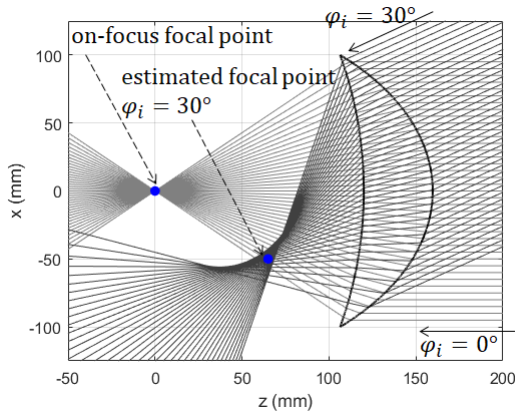


FIGURE 11. On-focus and 30° off-focus receiving mode ray tracing of Abbe's sine condition lens.

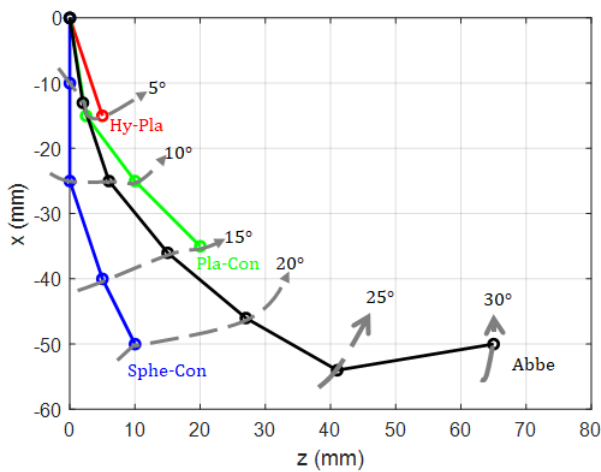


FIGURE 12. Summary of estimation of feed positions.

C. DETERMINATION OF FEED POSITION

1) MINIMUM AVERAGE DISTANCE

Determining the feed position for rays that are off-focus and diverged is not easy, hence a robust selection mechanism is proposed. The decision is made by employing a minimum average distance selection mechanism. This mechanism considers the ray density by calculating the distance of a point with all the rays.

Some test points are made as shown in Fig. 13. The distance between each test point and the focal region ray is calculated. Each line  $l_j$  can be expressed as another form of (14) by general expression [30], [31], [32], [33]

$$x = m_j z + c_j \tag{15}$$

where  $m_j = \tan \phi_j$  is gradient and  $c_j$  is a constant of each ray. Therefore, the distance of test point  $(z_k, x_k)$  and the ray  $l_j$  can be calculated as

$$d_{jk} = \frac{|-m_j z_k + x_k - c_j|}{\sqrt{m_j^2 + 1}} \tag{16}$$

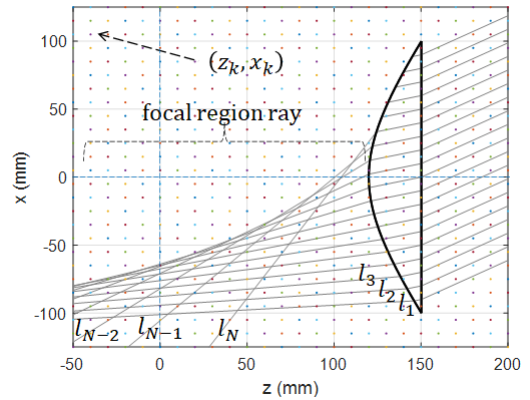


FIGURE 13. Scheme of feed position determination.

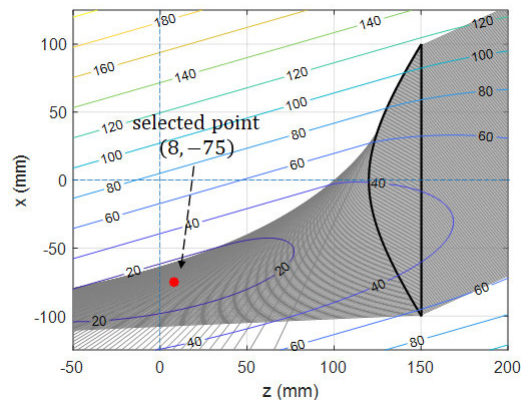


FIGURE 14. Feed position determination of hyperbolic-planar lens at 30° incident angle.

The distance is calculated for each test point  $(z_k, x_k)$  and ray  $l_j$ .

To decide on a point with a minimum average distance, a calculation of the average distance of each point with all rays is required. The average distance is

$$\bar{d}_k = \frac{\sum_{j=1}^N d_{jk}}{N} \tag{17}$$

with  $d_{jk}$  is the distance between point  $k$  with ray  $l_j$  and  $N$  is the number of the ray. Then, point  $k$  with  $\bar{d}_k$  which has the least value is selected. In this article,  $\Delta x = 1$  mm is used to obtain selection with high accuracies. Then, the scanning point interval is set to 1 at both the  $z$ -axis and  $x$ -axis.

Fig. 14 shows the result of the minimum average distance on a hyperbolic-planar lens at a 30° incident angle. The same distance value is shown by the contour. The smallest distance point is at  $(8, -75)$  coordinate. And the smallest distance at this point is 13.6457 mm.

2) MINIMUM AVERAGE DISTANCE VALUE

The increase of the minimum average distance for the incident angle is summarised in Fig. 15. The distance becomes largest at the hyperbolic-planar lens, and the distance becomes smallest at Abbe's sine condition lens.

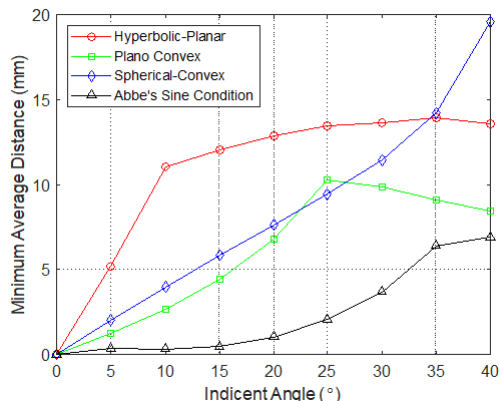


FIGURE 15. Value of the minimum average distance for each lens types.

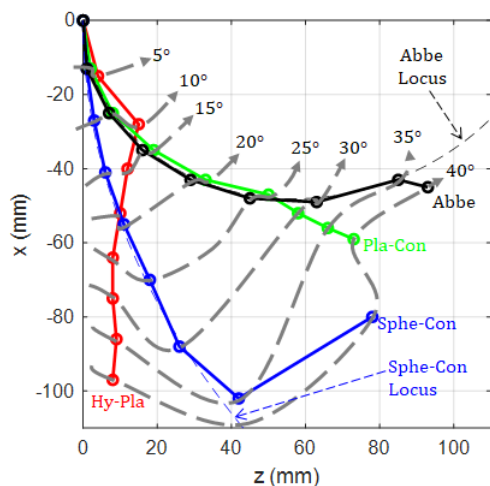


FIGURE 16. The coordinates of minimum average distance points.

At a 30° incident angle, the minimum average distance becomes 6.9133 mm. In the case of Abbe’s sine condition, the minimum average distance is rather small as shown in Fig. 11 showing that good focusing characteristics are obtained. In the case of the hyperbolic-planar, plano-convex, and spherical-convex, the very large spread of the focal region rays, the minimum average distance gives information that the rays are very diverged.

Calculation of the minimum average distance involves the total distance of the respected point to all rays. It is the cause of some irregularities in the minimum average distance value. At some incident angles, the total internal reflection on the inner surface of the lens is obtained. Therefore,  $N$  in (17) becomes lower due to the limited number of refracted rays. It explains how at some point, the trend of the minimum average distance becomes irregular.

### 3) FEED POSITION

The coordinate points of the minimum average distance points are shown in Fig. 16. In the case of the hyperbolic-planar (Hy-Pla) lens, the minimum distance points are distributed near the z-axis. In the case of the spherical-convex (Sphe-Con) lens, the minimum distance points stay at the

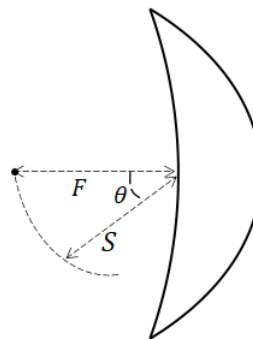


FIGURE 17. Locus of Abbe’s sine condition.

middle of the x-axis and the z-axis. Meanwhile, in the case of Abbe’s sine condition (Abbe) and plano-convex (Pla-Con) lenses, the minimum distance points distribute near the locus of Abbe’s sine condition

$$S = F (\cos \theta)^2 . \tag{18}$$

Here,  $F$  is the focal length and  $S$  is the distance to the locus point as shown in Fig. 17. While for other lens, such as spherical-convex, locus can be described as

$$S = F (\cos \theta)^{-0.2} . \tag{19}$$

Generally, feed position locus is

$$S = F (\cos \theta)^\alpha \tag{20}$$

with varying  $\alpha$  depend on the lens shape.

In some cases, a good pattern of feed position is expected, such as a nearly linear or smooth curving feed position. A nearly linear feed position may ease the configuration of feed antennas by a planar array. A smooth curving feed position is also easy to configure by a curving array antenna. Therefore, a well-defined locus is important as shown in (20). As for a low curvature of locus,  $\alpha$  is a small number.

The results of Fig. 16 give important information for the best feed positions. The minimum average distance point is suitable for the best feed position and will be used for the next step of electromagnetic simulations.

## IV. ELECTROMAGNETIC SIMULATION

Electromagnetic simulations of the multibeam radiation patterns are very important for the validation of the four types of lens antenna features. In this section, configurations of electromagnetic simulation are explained.

### A. ELECTROMAGNETIC SIMULATOR

FEKO is used for electromagnetic simulation. The simulation parameter of the employed FEKO simulator is presented in Table. 2. A high-performance computer is used to ensure the accuracy and efficiency of the running time. The Multilevel Fast Multipole Method (MLFMM) is used for speeding up the calculation time considering the antenna’s geometry. Simulation is conducted at 28 GHz frequency which is the designated frequency of the antenna.

TABLE 2. Simulation parameter.

Computer Processor	Intel Xeon E5-2683 v4 2.10 GHz
Random Access Memory	512 GB 2400 MHz
Software	
Electromagnetic Simulation	FEKO 2019.2
Method	Method of Moment (MoM) - Multilevel Fast Multipole Method (MLFMM)
Frequency	28 GHz
Mesh Size	0.05λ
Calculation Time	±30 minutes

TABLE 3. Beam shifting of multibeam radiation pattern.

Beam	Expected Beam Shifting (°)	Obtained Beam Shifting (°)			
		Hy-Pla	Pla-Con	Sphe-Con	Abbe
B <sub>0</sub>	0	0	0	0	0
B <sub>1</sub>	5	5.6	5.1	5.1	5.1
B <sub>2</sub>	10	10.2	10	10.4	10.1
B <sub>3</sub>	15	15.5	15	15.4	14.9
B <sub>4</sub>	20	20.2	20.4	20.4	20
B <sub>5</sub>	25	25.7	26	25.3	25.2
B <sub>6</sub>	30	29.8	30.2	30.6	30.4
B <sub>7</sub>	35	34.4	35.9	35.4	36
B <sub>8</sub>	40	40	40.4	-	39.4

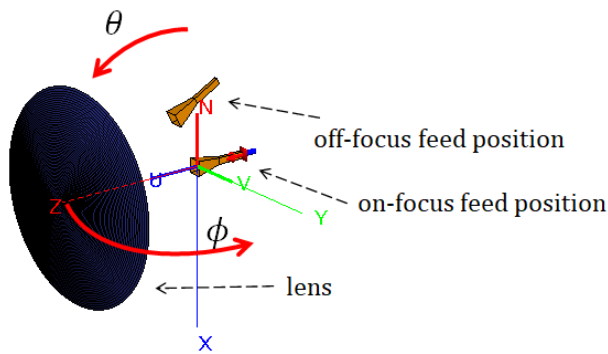


FIGURE 18. Lens and feed configuration.

12.04 dBi gain. Radiation patterns of the horn are shown in Fig. 19b. The beamwidth is 44.42° and 48.58° for E-Plane and H-Plane, respectively.

V. MULTIBEAM RADIATION PATTERN RESULTS

In this section, the best multibeam antenna will be found from the four types of lens antennas. First of all, 3D main beam shapes at different beam directions are obtained to make clear the differences between the four types of antennas. Then, the detailed beam shape changes and the gain changes at different beam directions are shown in 2D radiation patterns. Finally, the gain performance and sidelobe comparison are presented.

Each multibeam radiation pattern is marked as B = {B<sub>0</sub>, B<sub>1</sub>, B<sub>2</sub>, ..., B<sub>8</sub>} with expected beam shifting as shown in Table 3. The obtained beam shifting is the direction where the peak of radiation pattern located. These beams achieved maximum 1° deviation from the expected shifting angle. Considering that each beam has beamwidth more than 3°, the expected shifting angle is in the half-power beam area. Therefore, the beamshifting is considered accurate. More detail explanation from 3D radiation pattern is presented in Subsection V-A. Then, explanation about beam shape and gain change is presented in Subsection V-B. After that, gain reduction is explained in Subsection V-C. Additionally, sidelobe level of each multibeam radiation pattern is presented in Subsection V-D.

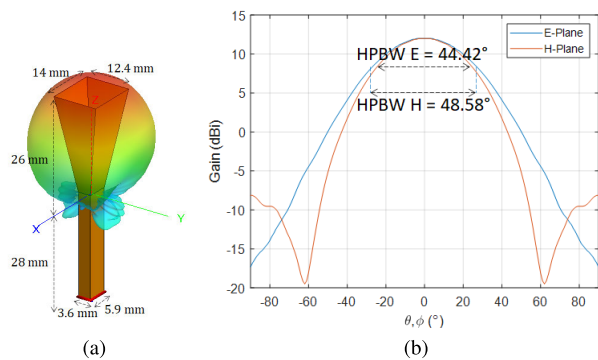


FIGURE 19. Feed horn: (a) geometry, (b) radiation pattern.

B. SIMULATION GEOMETRY

The geometry of the lens antenna and feed positions are shown in Fig. 18. Feed horns are placed on the zx-plane wherein, multibeam directions are shown by the angle theta. Feed horn positions for the multibeam are determined based on the xz-coordinate shown in Fig. 16. Practically, this feed horn can be replaced with another feed antenna, such as a patch array antenna. The feed antenna should have a sufficient portion of the beam within the lens area to illuminate the lens surface. Therefore, a good multibeam radiation pattern is obtained.

C. FEED HORN MODEL

The geometry of the horn antenna is shown in Fig. 19a. A pyramidal horn of aperture sizes 14 mm x 12.4 mm. This horn has a unidirectional radiation pattern with a

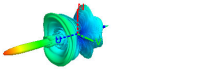
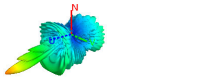
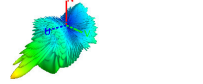
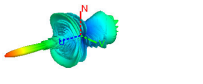
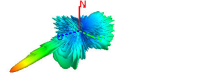
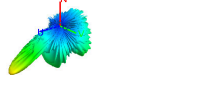
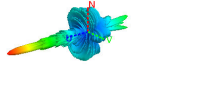
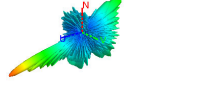
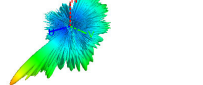
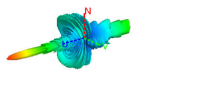
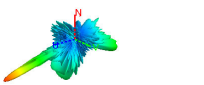
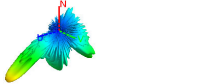
A. 3D RADIATION PATTERN

The multibeam radiation patterns of the hyperbolic-planar, plano-convex, spherical convex, and Abbe's sine condition lenses are shown in Table. 4. Main beam directions of 0°, 15°, and 30° are shown.

All lenses show a good pencil beam at 0° direction. At a beam direction of 15°, the main beamwidth of the hyperbolic-planar types becomes wider than the other three types. At a beam direction of 30°, the sharpest beamwidth is achieved by the spherical-convex type. To clarify the beam shape, radiation intensities in theta-phi-coordinate at 30° beams are shown in Fig. 20. The main beam shape differences become clear. The spherical-convex type achieves the most excellent pencil beam. At the hyperbolic-planar type, the main beam becomes wide in the theta direction. At the plano-convex and



TABLE 4. Multibeam radiation pattern results.

Lens Shape	$B_0(0^\circ)$	$B_3(15^\circ)$	$B_6(30^\circ)$
Hyperbolic-Planar			
Plano-Convex			
Spherical-Convex			
Abbe's Sine Condition			

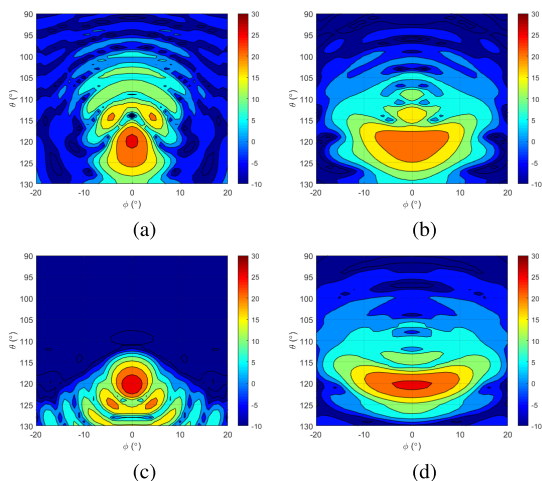


FIGURE 20. Radiation intensities at 30° beam: (a) hyperbolic-planar lens, (b) plano-convex lens, (c) spherical-convex lens, (d) Abbe's sine condition lens.

Abbe's sine condition types, the main beam spreads in the  $\phi$  direction. Detailed main beam shapes become clear.

**B. BEAM SHAPE AND GAIN CHANGES**

Detailed beam shape changes and gain change in the  $\theta$  direction are shown at  $\theta$  with an increment of 5°. The antenna type with the smallest gain changes is clarified.

1) HYPERBOLIC-PLANAR LENS

The multibeam radiation patterns of the hyperbolic-planar lens are shown in Fig. 21. The beam direction of 0° produces the highest gain of 32.31 dBi. The main beam shape deformation begins at 10° beam and deformation becomes larger as the beam direction increases. The gain reduction from 0° to 35° becomes -7.91 dB.

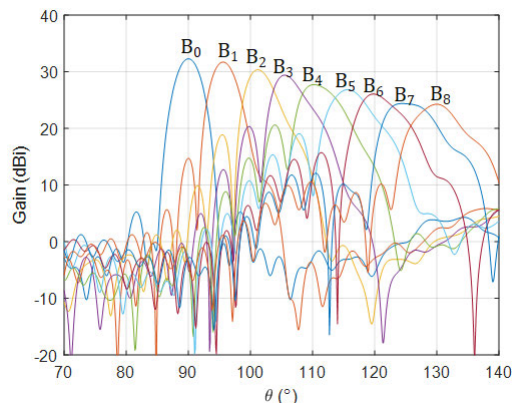


FIGURE 21. 2D multibeam radiation pattern of the hyperbolic-planar lens.

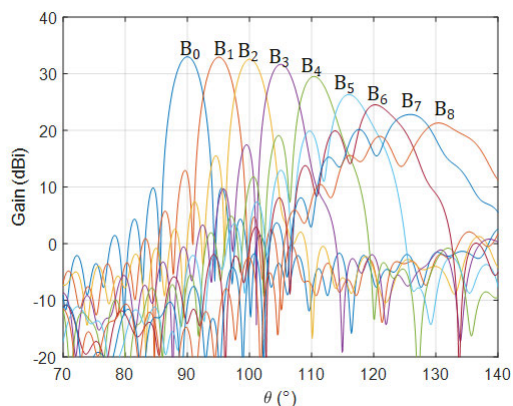


FIGURE 22. 2D Multibeam radiation pattern of the plano-convex lens.

2) PLANO-CONVEX LENS

The multibeam radiation pattern of the plano-convex lens is shown in Fig. 22. A beam direction of 0° produces the highest gain of 33.01 dBi. The main beam shape

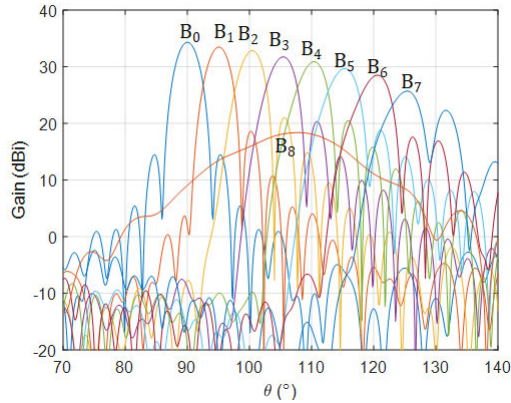


FIGURE 23. 2D multibeam radiation pattern of the spherical-convex lens.

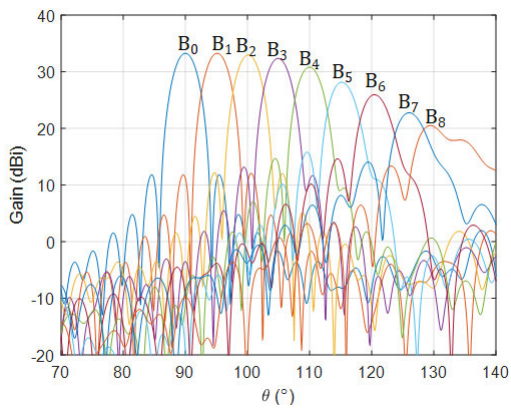


FIGURE 24. 2D multibeam radiation pattern of Abbe's sine condition lens.

deformation begins at 25° beam and deformation becomes larger as the beam direction increases. The deformation angle of the beam direction of this lens is better than the hyperbolic-planar. However, the gain reduction from 0° to 35° becomes -10.19 dB, which is comparable to the hyperbolic-planar lens.

### 3) SPHERICAL-CONVEX LENS

Multibeam radiation patterns of the spherical-convex lens are shown in Fig. 23. This lens can achieve high gain at 0° beam direction with a value of 34.33 dBi. The main beam shape deformations begin at 30° beam, which is considered wide. The gain reduction from 0° to 35° beam becomes -8.61 dB.

### 4) ABBE'S SINE CONDITION LENS

The multibeam radiation patterns of the Abbe's sine condition lens are shown in Fig. 24. The maximum gain is achieved at 0° with a value of 33.28 dBi. The main beam shape deformations begin at 30° beam. The gain reduction from 0° to 35° beam becomes -10.49 dB.

### C. GAIN REDUCTION IN MULTIBEAM

A summary of the gain reductions in multibeam is shown in Fig. 25. The spherical-convex lens achieves the highest

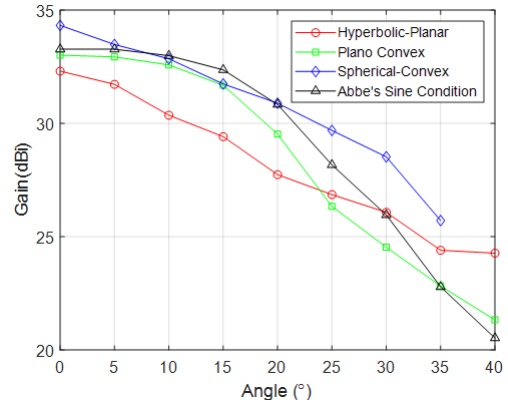


FIGURE 25. Gain comparison of hyperbolic-planar, plano-convex, spherical-convex, and Abbe's sine condition lenses.

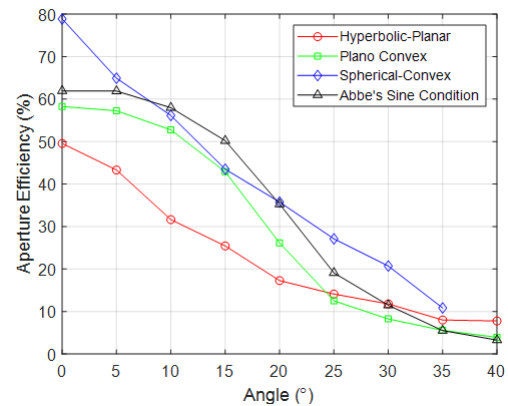


FIGURE 26. Aperture efficiency of hyperbolic-planar, plano-convex, spherical-convex, and Abbe's sine condition lenses.

gain at 0° to 35°. At 0° beam, the antenna gain of 34.33 dBi is achieved. By comparing the maximum theoretical gain of 35.36 dBi, the gain reduction is only -1.03 dB. The second highest gain type is Abbe's sine condition lens. The third in order is the plano-convex lens. The hyperbolic-planar lens becomes the fourth in order. Antenna gain reductions from the maximum gain in the form of aperture efficiency are shown in Fig. 26. Overall, the spherical convex type achieves the highest aperture efficiency. At 0°, aperture efficiency of 78.88% is achieved and at 10° it is maintained around 56.16%.

### D. SIDELobe LEVEL

The summary of the sidelobe level is shown in Fig. 27. At 0° on focus beam direction, all lenses show good sidelobe level. Sidelobe levels are increased gradually with a higher angle beam direction. A lower sidelobe level is better. Abbe's sine condition lens shows the best sidelobe level compared to other lens shapes. The sidelobe level of Hyperbolic-planar starts to decrease at 20° and above beam direction. It achieves the lowest sidelobe level at 35° and 40° beam direction. As for the spherical-convex lens, the value is relatively constant

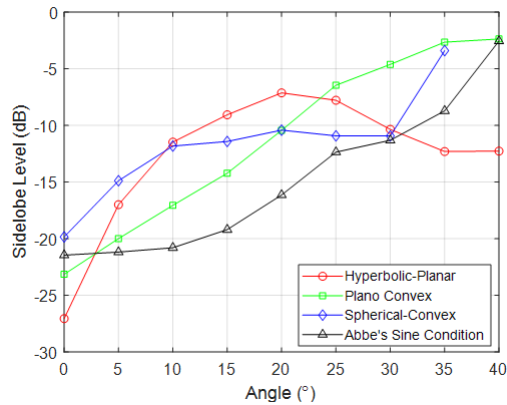


FIGURE 27. Sidelobe level comparison of hyperbolic-planar, plano-convex, spherical-convex, and Abbe's sine condition lens.

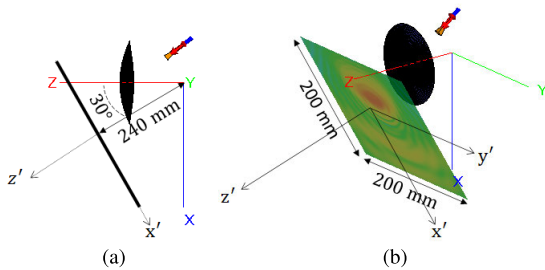


FIGURE 28. Near Field Aperture Plane for 30° beam direction: (a) xz-view, (b) 3D view.

from 10° to 30° beam direction. While for plano-convex, the sidelobe level is constantly increasing.

## VI. DISCUSSION

In this section, a discussion of near-field distribution and changes on  $F/D$  are presented. Near-field distribution explains the performance of the lens antenna. While changing the  $F/D$  to lens design and changing lens material might change lens performance.

### A. NEAR FIELD DISTRIBUTION

Results of far-field radiation pattern and gain are good data for evaluating multibeam characteristics of four types of lens antenna. These results can be explored in more detail using aperture plane electric fields. In Fig. 28, the aperture plane for 30° is shown. Here, the aperture plane is set perpendicular to the beam axis to clarify amplitude and phase distribution on the aperture plane. The strong homogeneous electric field inside the lens area demonstrates good amplitude distribution. The uniform electric phase inside the lens area indicates good phase distribution. As a result, high aperture efficiency, constructive refraction, and optimum gain can be achieved.

In Fig. 29, amplitude distributions of the electric fields on the  $x'y'$ -plane are shown. The black circles indicate the projections of the lens antenna's rims. For the hyperbolic-planar type, the large amplitude area is concentrated at the central area in the lens rim. For the plano-convex and Abbe's

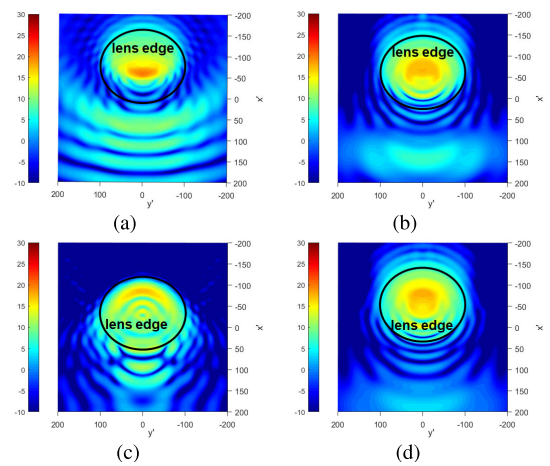


FIGURE 29. Electric field amplitude distribution on the 30° beam aperture plane: (a) hyperbolic-planar lens, (b) plano-convex lens, (c) spherical-convex lens, (d) Abbe's sine condition lens.

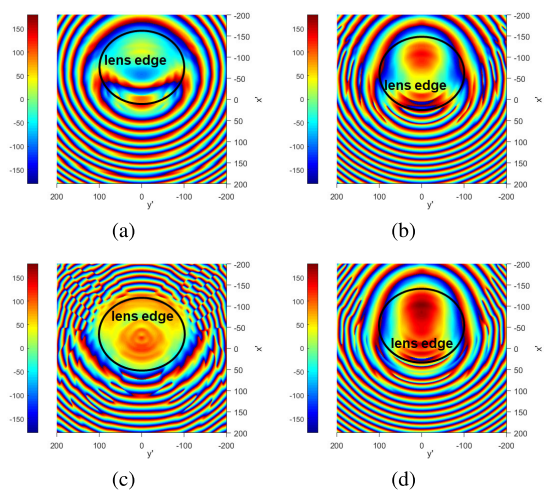


FIGURE 30. Electric field phase distribution on the 30° beam aperture plane: (a) hyperbolic-planar lens, (b) plano-convex lens, (c) spherical-convex lens, (d) Abbe's sine condition lens.

sine condition types, the large amplitude areas spread wide in the lens rim. And for the spherical-convex type, the large amplitude areas are spread more widely in the lens rim. The amplitude distribution of the spherical convex is the flattest. So, a high aperture efficiency is expected. As for Abbe's sine condition lens, the amplitude is distributed densely within the lens area. It explains the obtained low sidelobe.

In Fig. 30, the phase distribution in the  $x'y'$ -plane is shown. At the hyperbolic-planar type, a large phase change is observed in the  $x'$  axis direction. At the plano-convex and Abbe's sine types, large phase changes are observed in  $y'$  axis. At the spherical-convex type, the phase change becomes the smallest in the lens rim. The phase change from its maximum to its minimum becomes within 50°. Good amplitude and phase distribution of the spherical-convex type produce a gain increase of 2.5 dB at a 30° beam, as shown in Fig. 25.

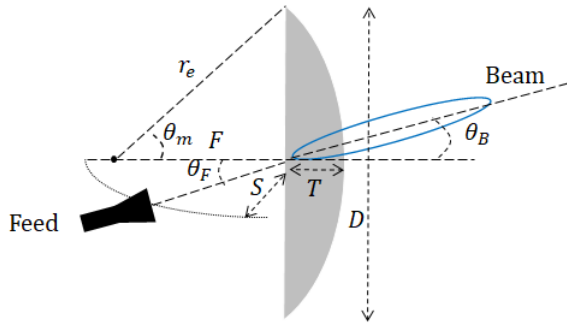


FIGURE 31. Corresponding feed angle and beam direction.

TABLE 5. Impact of F/D change.

F/D	Low	0.6 Sample: Abbe	High
<b>Lens Geomtery</b>			
$\theta_m$	High	43.23 mm	Low
$r_e - F$	Large	26 mm	Small
Lens Thickness (T)	Thick	39.62 mm	Thin
<b>Focusing Ability</b>			
Ray Concentration	More Diverged	Diverged	Less Diverged
$\min(d_k)$ of Eq. (17)	Large	3.69 mm at 30°	Small
Field of View	Narrow-Angle	$\approx 35^\circ$	Wide-Angle
Feed Position (S)	$F(\cos \theta_F)^\alpha$	$F(\cos \theta_F)^\alpha$	$F(\cos \theta_F)^\alpha$

**B. THE INFLUENCE OF F/D CHANGE**

Some lens geometries become crucial for producing good multibeam radiation patterns, as seen in Fig. 31. To achieve  $\theta_B$  beam direction, the feed antenna is positioned at the focal point of each beam direction with  $\theta_F$  angle. In this case,  $\theta_F \approx \theta_B$  is achieved.

Table. 5 summarizes the effect of changing the F/D ratio on focusing properties. The focusing abilities are strongly depending on the lens thickness. Firstly, lens thickness is changed by F/D change. At a thick lens, focusing will be weakened, then focusing is more diverged. At a thin lens, focusing will be strong, then focusing are less diverged. The focusing ability determines the coverage angle (field of view). A good focusing lens may be applied to obtain a wide coverage angle. F/D changes affect feed position. However, the feed locus S is depending on only F value.

To visualize the effect of F/D change, ray convergences of Abbe’s sine condition lens with  $F/D = 0.6$  and  $F/D = 1.0$  are shown in Fig. 32. A lens with  $F/D = 1.0$  is thinner than  $F/D = 0.6$ . It then affects the lens’ focusing. For higher  $F/D - 1.0$ , the concentrating area is smaller than  $F/D = 0.6$ .

**C. THE INFLUENCE OF REFRACTIVE INDEX CHANGE**

The lens thickness will change as the refractive indexes of the lens material change. Lens thickness decreases at higher n values, allowing better focusing ability. When the n value is low, the lens becomes thick and the focusing ability is reduced. Fig. 33 shows the Abbe’s sine condition lens with  $n = 1.6$  and  $n = 2$ . A lens with  $n = 1.6$  has a larger focal region than a lens with  $n = 2$ . This focusing ability has an impact on the coverage angle. As a result, at higher n values,

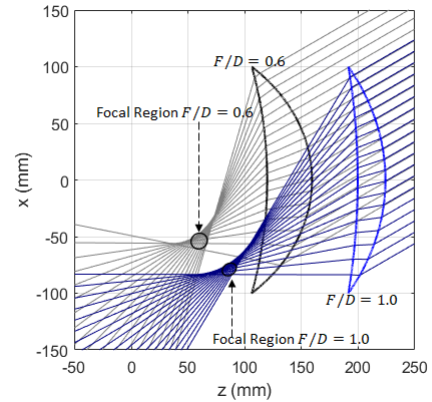


FIGURE 32. Focal region of Abbe’s sine condition lens with  $F/D = 0.6$  and  $1.0$  at 30° angle.

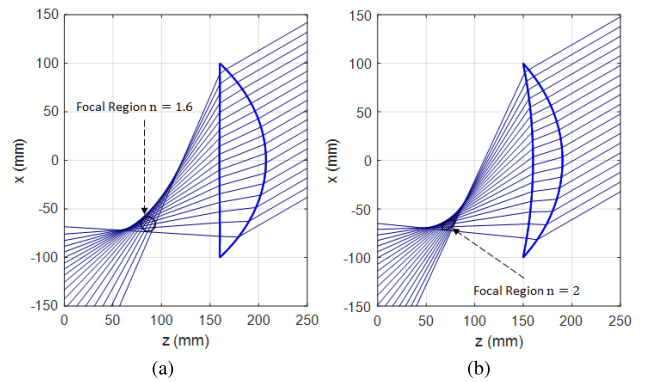


FIGURE 33. Focal region of Abbe’s sine condition lens at 30° angle: (a)  $n = 1.6$ , (b)  $n = 2$ .

a wider coverage angle is achievable. However, for a high refractive angle material, there will be higher reflection on the lens surface due to high refractive index differences between air and the lens. Therefore, for practical usage, choosing lens material should consider this trade-off.

**D. FEED DISPLACEMENT**

In this research, it is shown that the best feed position of any lens shape can be found by using focal region ray tracing explained in Section III. Any displacement from these found feed positions may reduce the obtained gain and move the beam direction. Feed displacement can be occurred in angular or radial position as shown in Fig. 34. Impact of feed displacement is explained in this Subsection.

Angular displacement of the spherical-convex lens at 20° beam direction is shown in Fig. 35. The feed is displaced by 5° from its initial best position. It is shown that the beam direction is shifted. Therefore, if the feed is displaced from its original best feed position by angular displacement, the obtained beam direction may not be accurate.

Radial displacement of the spherical-convex lens at 20° beam direction is shown in Fig. 36. The feed is displaced by 1 cm from its initial best position. It is shown that

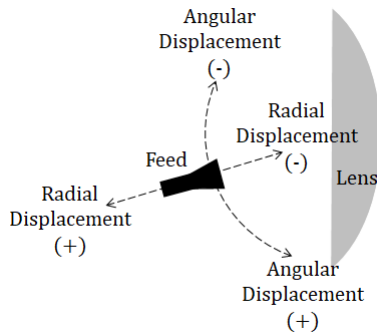


FIGURE 34. Angular and radial feed displacement.

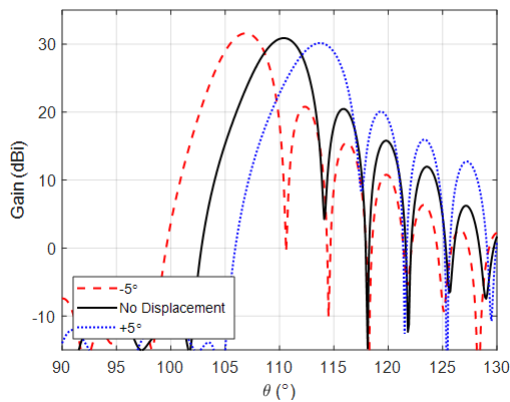


FIGURE 35. Radiation pattern of angular feed displacement on the spherical-convex lens at 20° beam.

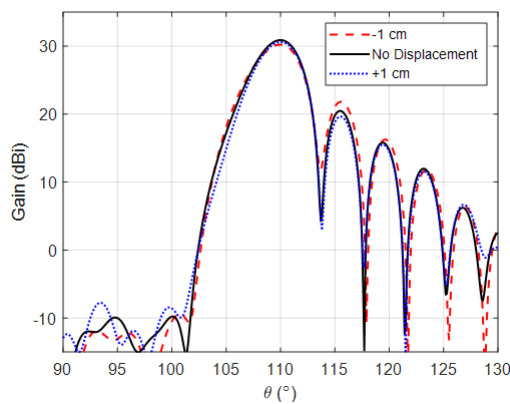


FIGURE 36. Radiation pattern of radial feed displacement on the spherical-convex lens at 20° beam.

the gain is reduced by 0.67 dB and 0.19 dB for feed displacement of  $-1$  cm and  $+1$  cm, respectively. Therefore, if the feed is displaced from its original best feed position by radial displacement, the obtained gain may not be optimum. The gain change over radial feed displacement for the spherical-convex lens at  $20^\circ$  beam direction is summarized in Fig. 37. It is shown that at the selected feed position (0 radial displacement), the achieved gain is maximum. It validates that the feed position obtained in Section III is the best feed position.

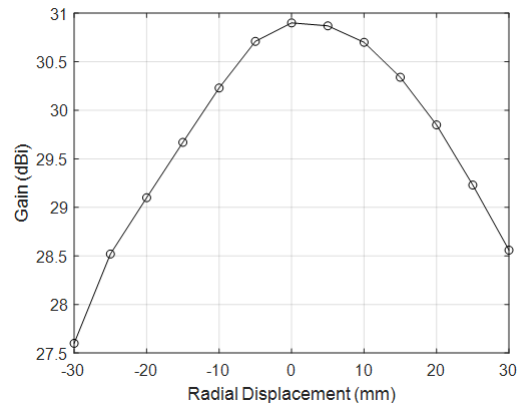


FIGURE 37. Summary of radial feed displacement on the spherical-convex lens at 20° beam.

## VII. CONCLUSION

To find out the best multibeam lens antenna, the typical three antenna types such as hyperbolic-planar, plano-convex, and spherical convex were selected. Moreover, the shaped lens type like Abbe's sine condition which is well known for its good multibeam radiation characteristics was also considered. The prime concern was to find out the best feed positions for the multibeam performance. Two MATLAB programs were developed. The first program was to achieve a focal region ray for the slant incident ray. Through using this program, the focal region ray's spread for the incident ray angle increment was shown to have increased. The second program was to find out the smallest distant point from all focal region rays. Through this program, suitable feed position data for the feed positions were obtained. Based on the obtained feed position data, multibeam radiation patterns were obtained by electromagnetic simulations. The main beam shape deformations from a pencil beam, the beamwidth changes, and the gain reductions depended on beam directions of  $0^\circ - 25^\circ$  were shown.

Of the four types of antennas, the spherical convex type achieved the highest gain and the best beam shape. To understand the reason, aperture distributions at  $30^\circ$  beam were compared between the four antenna types. The spherical-convex type achieved a flat amplitude and constant phase distributions. The reason for the high and good beam shape had been made clear. In terms of sidelobe level, Abbe's sine condition lens presents the best performance with the lowest overall sidelobe level among other lenses. The obtained multibeam results of the four types of lenses would be useful for the selection of the best multibeam lens antenna. Moreover, a newly proposed method of finding out the best feed positions would be useful for feed design.

Modification of lens parameters is possible to create a feasible lens design. It then changes the focusing characteristics of the lens. By applying the correct adjustments, feed antenna separation will be sufficient. Additionally, improvement in beam coverage is also possible.

## REFERENCES

- [1] K.-C. Huang and Z. Wang, *Millimeter Wave Communication Systems*, vol. 29. Hoboken, NJ, USA: Wiley, 2011.
- [2] H. Y. Lam, L. Luini, J. Din, M. J. Alhilali, S. L. Jong, and F. Cuervo, "Impact of rain attenuation on 5G millimeter wave communication systems in equatorial Malaysia investigated through disdrometer data," in *Proc. 11th Eur. Conf. Antennas Propag. (EUCAP)*, Mar. 2017, pp. 1793–1797.
- [3] A. Alnoman and A. Anpalagan, "Towards the fulfillment of 5G network requirements: Technologies and challenges," *Telecommun. Syst.*, vol. 65, no. 1, pp. 101–116, May 2017.
- [4] J. Zhang, Y. Huang, T. Yu, J. Wang, and M. Xiao, "Hybrid precoding for multi-subarray millimeter-wave communication systems," *IEEE Wireless Commun. Lett.*, vol. 7, no. 3, pp. 440–443, Jun. 2018.
- [5] D. Jiang and G. Liu, "An overview of 5G requirements," in *5G Mobile Communications*. Cham, Switzerland: Springer, 2017, pp. 3–26.
- [6] I. F. Akyildiz, A. Kak, and S. Nie, "6G and beyond: The future of wireless communications systems," *IEEE Access*, vol. 8, pp. 133995–134030, 2020.
- [7] R. Chataut and R. Akl, "Massive MIMO systems for 5G and beyond networks—Overview, recent trends, challenges, and future research direction," *Sensors*, vol. 20, no. 10, p. 2753, May 2020.
- [8] M. A. Albreem, M. Juntti, and S. Shahabuddin, "Massive MIMO detection techniques: A survey," *IEEE Commun. Surveys Tuts.*, vol. 21, no. 4, pp. 3109–3132, 4th Quart., 2019.
- [9] J. Zhang, S. Chen, Y. Lin, J. Zheng, B. Ai, and L. Hanzo, "Cell-free massive MIMO: A new next-generation paradigm," *IEEE Access*, vol. 7, pp. 99878–99888, 2019.
- [10] M. Muhsin and R. Pudji, "Dual-cross-polarized antenna decoupling for 43 GHz planar massive MIMO in full duplex single channel communications," *Int. J. Adv. Comput. Sci. Appl.*, vol. 10, no. 4, pp. 364–370, 2019.
- [11] M. Muhsin, A. L. Nurlaili, A. Saharani, and I. R. Utami, "Sectoral dual-polarized MIMO antenna for 5G-NR band N77 base station," *Indonesian J. Electr. Eng. Comput. Sci.*, vol. 21, no. 3, pp. 1611–1621, Mar. 2021.
- [12] T. Elkarkraoui, M.-R. Nezhad-Ahmadi, and S. Safavi-Naeini, "A high gain beam-steering Luneburg lens antenna for 76–81 GHz automotive radars," in *Proc. IEEE Int. Symp. Antennas Propag. North Amer. Radio Sci. Meeting*, Jul. 2020, pp. 1615–1616.
- [13] Y. Guo, Y. Li, J. Wang, L. Ge, Z. Zhang, M. Chen, Z. Li, B. Ai, and R. He, "A 3D printed nearly isotropic Luneburg lens antenna for millimeter-wave vehicular networks," *IEEE Trans. Veh. Technol.*, vol. 71, no. 2, pp. 1145–1155, Feb. 2022.
- [14] Y. Su and Z. N. Chen, "A flat dual-polarized transformation-optics beams scanning Luneburg lens antenna using PCB-stacked gradient index metamaterials," *IEEE Trans. Antennas Propag.*, vol. 66, no. 10, pp. 5088–5097, Oct. 2018.
- [15] Y. Su, Z. N. Chen, and A. K. Skrivervik, "A compact transformation optics-based Luneburg lens antenna using curved reactive impedance surface," in *Proc. 15th Eur. Conf. Antennas Propag. (EuCAP)*, Mar. 2021, pp. 1–4.
- [16] E. Garcia-Marin, D. S. Filipovic, J. L. Masa-Campos, and P. Sanchez-Olivares, "Low-cost lens antenna for 5G multi-beam communication," *Microw. Opt. Technol. Lett.*, vol. 62, no. 11, pp. 3611–3622, Nov. 2020.
- [17] H. Giddens and Y. Hao, "Multibeam graded dielectric lens antenna from multimaterial 3-D printing," *IEEE Trans. Antennas Propag.*, vol. 68, no. 9, pp. 6832–6837, Sep. 2020.
- [18] H. Luh, T. Smith, and W. Scott, "A dual-band TEM lens for a multiple beam antenna system," *IEEE Trans. Antennas Propag.*, vol. AP-30, no. 2, pp. 224–229, Mar. 1982.
- [19] Y. T. Lo and S. Lee, *Antenna Handbook: Theory, Applications, and Design*. New York, NY, USA: Springer, 2013.
- [20] P. Piksa, S. Zvanovec, and P. Cerny, "Elliptic and hyperbolic dielectric lens antennas in mm-Waves," *Radioengineering*, vol. 20, no. 1, pp. 270–275, Apr. 2011.
- [21] K. Hongo and H. Kobayashi, "Radiation characteristics of a plano-convex lens antenna," *Radio Sci.*, vol. 31, no. 5, pp. 1025–1035, Sep. 1996.
- [22] T. Tajima, Y. Yamada, S. Sasaki, and A. Kezuka, "Calculation of wide angle radiation patterns and caustics of a dielectric lens antenna by a ray tracing method," *IEICE Trans. Electron.*, vol. 87, no. 9, pp. 1432–1440, Sep. 2004.
- [23] F. Ansarudin, T. A. Rahman, Y. Yamada, N. H. A. Rahman, and K. Kamardin, "Multi beam dielectric lens antenna for 5G base station," *Sensors*, vol. 20, no. 20, p. 5849, Oct. 2020.
- [24] A. L. Peebles, "A dielectric bifocal lens for multibeam antenna applications," *IEEE Trans. Antennas Propag.*, vol. 36, no. 5, pp. 599–606, May 1988.
- [25] T. Maruyama, K. Yamamori, and Y. Kuwahara, "Design of multibeam dielectric lens antennas by multiobjective optimization," *IEEE Trans. Antennas Propag.*, vol. 57, no. 1, pp. 57–63, Jan. 2009.
- [26] B. Schoenlinner, X. Wu, J. P. Ebling, G. V. Eleftheriades, and G. M. Rebeiz, "Wide-scan spherical-lens antennas for automotive radars," *IEEE Trans. Microw. Theory Techn.*, vol. 50, no. 9, pp. 2166–2175, Sep. 2002.
- [27] N. T. Nguyen, A. V. Boriskin, L. Le Coq, and R. Sauleau, "Improvement of the scanning performance of the extended hemispherical integrated lens antenna using a double lens focusing system," *IEEE Trans. Antennas Propag.*, vol. 64, no. 8, pp. 3698–3702, Aug. 2016.
- [28] M. Jiang, Z. N. Chen, Y. Zhang, W. Hong, and X. Xuan, "Metamaterial-based thin planar lens antenna for spatial beamforming and multibeam massive MIMO," *IEEE Trans. Antennas Propag.*, vol. 65, no. 2, pp. 464–472, Feb. 2017.
- [29] S. Silver, *Microwave Antenna Theory and Design*, no. 19. Edison, NJ, USA: IET, 1984.
- [30] R. Larson, *Precalculus: A Concise Course*. Boston, MA, USA: Cengage Learning, 2013.
- [31] B. Spain, *Analytical Conics*. Chelmsford, MA, USA: Courier Corporation, 2007.
- [32] K. J. Smith, *Precalculus: A Functional Approach to Graphing and Problem Solving*. Burlington, MA, USA: Jones & Bartlett Publishers, 2011.
- [33] D. Cohen, T. B. Lee, and D. Sklar, *Precalculus*. Boston, MA, USA: Cengage Learning, 2016.



**M. MUHSIN** (Member, IEEE) received the bachelor's and master's degrees in telecommunications engineering from Telkom University, Bandung, Indonesia, in 2016 and 2017, respectively, and the Ph.D. degree from Universiti Teknologi Malaysia (UTM), Malaysia, in 2023. In 2018, he joined Telkom University Surabaya, Indonesia, where he has been an Assistant Professor. His research interests include wireless communications, antennas, and signal processing.



**KAMILIA KAMARDIN** (Senior Member, IEEE) received the B.Eng. degree in electronic (communications) from The University of Sheffield, U.K., in 2004, the M.Sc. degree in information technology (data communications and networking) from Universiti Teknologi Mara (UiTM), Malaysia, in 2007, and the Ph.D. degree in electrical engineering (communications) from Universiti Teknologi Malaysia (UTM), Malaysia, in 2014. She spent three months with the University of Birmingham, U.K., as a Visiting Ph.D. Student. Previously, she has served as a Senior Assistant Researcher with TM Research and Development, Malaysia for three years. Currently, she serves as a Senior Lecturer with the Department of Electronic Systems Engineering, Malaysia-Japan International Institute of Technology (MJIIT), UTM Kuala Lumpur. She is also an Associate Member of the Wireless Communication Centre (WCC). She is the Treasurer for IEEE Malaysia AP/MTT/EMC Joint Chapter, from 2018 to 2022. She is also a Professional Engineer registered under Board of Engineers Malaysia and a Professional Technologist under Malaysia Board of Technologist. Her research interests include antennas and propagation, body centric communication, antennas for 5G and beyond, metamaterials, and the Internet of Things (IoT).



**YOSHIHIDE YAMADA** (Senior Member, IEEE) received the B.S. and M.S. degrees in engineering from the Nagoya Institute of Technology, in 1971 and 1973, respectively, and the D.E. degree in electrical engineering from the Tokyo Institute of Technology, in 1989. He joined Electrical Communication Laboratories, Nippon Telegraph and Telephone Corporation (NTT), in 1973, and moved to NTT Mobile Communications Network Inc., (NTT DoCoMo), in 1993. In 1998, he joined National Defense Academy, as a Professor. In 2014, he joined the Malaysia-Japan International Institute of Technology, Universiti Teknologi Malaysia (UTM), Malaysia, as a Professor. His research interests include aperture antennas, array antennas, very small antennas, and radar cross sections. He is a fellow of the IEICE Japan, a Senior Member of IEEE APS, and a member of ACES. He received the Excellent Paper Award and the Best Tutorial Paper Award from IEICE, in 2013 and 2014, respectively.



**YOSHIKI SUGIMOTO** (Member, IEEE) was born in Fukui, Japan. He received the B.Sc. and M.Sc. degrees from the University of Fukui, Fukui, Japan, in 2013 and 2015, respectively, and the Ph.D. degree from Yokohama National University, Yokohama, Japan, in 2018. From 2018 to 2020, he was with Omron Corporation, where he was involved in the development of wireless power transfer systems and millimeter radar signal processing. In 2020, he joined the Nagoya Institute of

Technology as an Assistant Professor. His research interests include antenna measurement and scattering problems.



**KUNIO SAKAKIBARA** (Senior Member, IEEE) was born in Aichi, Japan, in 1968. He received the B.S. degree in electrical and computer engineering from the Nagoya Institute of Technology, Nagoya, Japan, in 1991, and the M.S. and D.E. degrees in electrical and electronic engineering from the Tokyo Institute of Technology, Tokyo, Japan, in 1993 and 1996, respectively. From 1996 to 2002, he was with Toyota Central Research and Development Laboratories Inc., Nagakute, where he was involved in the development of antennas for automotive millimeter-wave radar systems. From 2000 to 2001, he was a Guest Researcher with the Department of Microwave Techniques, University of Ulm, Ulm, Germany. In 2002, he joined the Nagoya Institute of Technology as a Lecturer. Since 2004, he has been an Associate Professor, and he became a Professor with the Nagoya Institute of Technology, in 2012. His current research interests include millimeter-wave and terahertz-wave antennas and feeding circuits.

• • •